# Optimisation of single contour strategy in selective laser melting of Ti-6Al-4V lattices

Cao, Xue; Carter, Luke; Villapun, Victor M.; Cantaboni, Francesco; De Sio, Giulia; Lowther, Morgan; Louth, Sophie; Grover, Liam; Ginestra, Paola; Cox, Sophie

*DOI:*
10.1108/RPJ-04-2021-0103



*Document Version*
Peer reviewed version

*Citation for published version (Harvard):*
Cao, X, Carter, L, Villapun, VM, Cantaboni, F, De Sio, G, Lowther, M, Louth, S, Grover, L, Ginestra, P & Cox, S 2022, 'Optimisation of single contour strategy in selective laser melting of Ti-6Al-4V lattices', *Rapid Prototyping Journal*, vol. 28, no. 5, pp. 907-915. https://doi.org/10.1108/RPJ-04-2021-0103

# Optimisation of Single Contour Strategy in Selective Laser Melting of Ti-6Al-4V Lattices

**Abstract:**

Purpose: Selective laser melting (SLM) is increasingly used to manufacture bone implants from titanium alloys with particular interest in porous lattice structures. These complex constructs have been shown to be capable of matching native bone mechanical behaviour leading to improved osseointegration while providing numerous clinical advantages, encouraging their broad use in medical devices. However, producing lattices with a strut diameter similar in scale to a typical SLM melt pool or using the same process parameters and scan strategies intended for bulk solid components may lead to geometric inaccuracies.

Methodology: Herein, we explore the potential of an unfilled single contour (SC) scanning strategy to improve the reproducibility of porous lattices when compared with a standard contour and fill approach (SC+F). For this purpose, two parametric analysis were carried out on Ti-6Al-4V diamond unit cell lattices with different strut sizes and scan strategies. Porosity and accuracy measurements were correlated with processing parameters and printing strategy to provide the optimal processing window for lattice manufacturing.

Findings: SC is shown to be a viable strategy for production of Ti-6Al-4V lattices with a strut diameter below 350 μm. Parametric analysis highlights the limits of this method in producing fully dense struts with energy density presented as a useful practical tool to guide some aspects of parameter selection (Design strut diameter achieved at ~ 0.1 J/mm in this study). Finally, a process map combining data from both parametric studies is provided to guide, predict and control lattice strut geometry and porosity obtained using the SC strategy.

Originality: These results explore the use of non-standard single contour (SC) scanning strategy as a viable method for producing strut-based lattice structures and compare against the traditional contour and fill approach (SC+F).

---

## 1. Introduction

Demand for orthopaedic implant surgery is predicted to exceed 5 million worldwide by 2021 with up to $65 billion in revenues estimated by 2025 (Murr, 2020). The freedom in design inherent to metal Additive Manufacturing (AM) and the expected rise in demand is stimulating research to add further functional properties to implantable devices boosting their application in medicine. In load-bearing implants, latticed structures have the potential to mimic the mechanical response of bone, reducing the stress shielding effect and limiting implant loosening (Hedayati *et al.*, 2018). These porous structures also have the potential to improve cell adhesion and osseointegration, thus strengthening the mechanical bond between patient and implant (Deing *et al.*, 2014, Maietta *et al.*, 2019). (Van Bael *et al.*, 2012) Finally, potential novel applications include the use of lattices as reservoirs to deliver antibiotics, growth factors, or other treatments directly to the implant site and MRI artefact mitigation (Burton *et al.*, 2019, Carter *et al.*, 2020). Nevertheless, in order to exploit these benefits, accuracy, predictability, and consistency of lattice production must be ensured.

Selective Laser Melting (SLM) is an AM technology whereby fully dense components are produced via layer-by-layer laser melting of metallic powder (Shipley *et al.*, 2018, Mullen *et al.*, 2009, Koptyug *et al.*, 2013). With a relatively high resolution and without traditional machining constraints, SLM presents a suitable method for production of components with integrated lattices. Part performance depends on the physicochemical properties of the powder feedstock and the SLM processing parameters. Powder quality is typically determined by supplier specification, however,

process parameters may be directly assigned by the SLM operator, heavily influencing the final part (Trevisan *et al.*, 2017). Laser power and scan speed represent two key process inputs (Song *et al.*, 2012, Nguyen *et al.*, 2020, Maamoun *et al.*, 2018) which control both melt pool size and shape further determining dimensional accuracy, microstructure, mechanical properties, and surface quality (Großmann *et al.*, 2019, Kusuma *et al.*, 2017). Energy density, $E$ (J/mm) as defined in Equation 1, combines these inputs to provide a simplified variable which may be useful in understanding certain behaviours (Yusuf and Gao, 2017, Kusuma *et al.*, 2017):

$$\boldsymbol{E} = \frac{\boldsymbol{P}}{\boldsymbol{V}} \text{ J/mm,} \qquad \textit{- Equation 1}$$

Where $P$ is laser power (W) and $v$ represents scan speed (mm/s).

The effect of $E$, $P$, and $v$ on surface roughness, porosity, and accuracy have been widely reported and trends linking process parameters to part quality identified (Hong *et al.*, 2016, Wang *et al.*, 2017, Khorasania *et al.*, 2019). Researchers have previously shown that increasing laser energy density and build angle induces greater surface roughness (Wang *et al.*, 2017, Qin and Chen, 2013, Villapún *et al.*, 2020), however, special care has been taken to understand the role of these inputs in internal porosity and defect type (Salem *et al.*, 2019). Porosity from trapped or evaporated gas in powder feedstock occurred at low scanning speed around 800 mm/s, while keyhole porosity is reportedly dominant at higher energy density conditions corresponding to a deep melt pool. Other reported defects include irregular and spherical shapes at high scan speed (2400-4000 mm/s) and lower laser power (100-300 W) due to melt track balling and lack of fusion. These results have been further supported by the work of Qiu *et al*. (Qiu *et al.*, 2015), although discrepancies on the optimal processing window can be found in the literature. This is highlighted by Gu *et al.* who showed internal porosity variations from 0% to 5.4% under a fixed "optimal" energy density (61 J/mm$^3$) by changing laser power and scan speed, suggesting that whilst energy density may be useful in some cases, the influence of individual parameters should not be overlooked (Gu *et al.*, 2013).

When processing fine lattice structures, strut thickness has been shown to significantly deviate from the initial CAD design. Yan *et al*. revealed up to 90 μm discrepancies with lattice strut design diameters between 420 μm and 610 μm (Yan *et al.*, 2014). This was confirmed by bulk analysis showing printed lattices being denser (10.66% and 13.12%) than the design (10% and 12%), which would lead to inconsistencies in mechanical properties between design and final part. A similar study found a linear relationship between lattice strut thickness and energy density with limited to no influence caused by scan strategy, build angle, or material, resulting in an increase in Young's modulus (Ghouse *et al.*, 2017). On the other hand, the work of Onal *et al*. suggests that these discrepancies in design rise with exposure time and laser power that subsequently stabilised for energy inputs above 0.5 J for produced lattices via a single point exposure scan strategy (Onal *et al.*, 2019).

The reported mismatch between design and manufactured geometry in these intricate structures is further complicated by the pre-processing software logic used to generate the laser path for each strut slice (Figure 1). The typical laser path for 250 μm strut slices shown in Figure 1b and 1f illustrates a 12% difference in energy input of neighbouring 'design identical' struts due to infill path planning. Additionally, scan spot placement between 'design identical' struts for both 150 μm and 350 μm show differences (Figure 1c and 1d). These inconsistencies between identically designed struts are likely to result in manufacturing inhomogeneities within a uniform lattice design. In contrast, the unfilled scan, figure 1a, shows consistent scan spots and path between adjacent struts (Figure 1e) for all diameters presenting a potentially more reliable method for lattice manufacture.

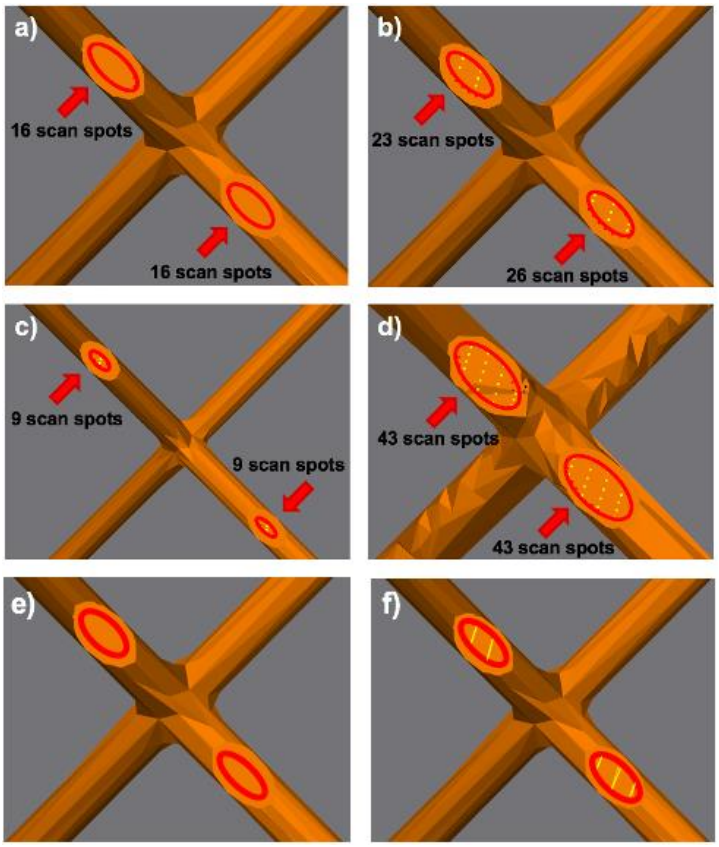


**Figure 1.** Images showing different number of scan spots in (a) SC and (b) SC+F strategies for designed struts size of 250 µm; (c) and (d) number of SC+F scan spots for 150 µm and 350 µm strut sizes; (e) scan path for SC scan; (f) scan path for SC+F. Red ellipsis represent border contours while yellow lines represent hatch (filling) scan.

In this paper, the accuracy of two scanning strategies, Single Contour (SC) (Figure 1e) and Single Contour plus Fill (SC+F) (Figure 1f), to manufacture SLM Ti-6Al-4V metal lattices was compared. during the manufacturing . Critical parameters, laser power and scan speed, were varied and lattice reproducibility, and integrity evaluated to determine an optimal processing window. Herein SC is revealed as a novel processing method with the potential to improve lattice accuracy of AM medical devices.

## 2. Materials and Methods

### *2.1. Materials and Specimen manufacturing*

. All cuboidal designs measured 20 x 20 x 20 mm with 1 mm unit cell (Figure 2a). CAD geometry was generated using nTopology Element (nTopology Inc., 1.25.0) design software, and exported as standard tessellation files (*.stl). (Nickels, 2020).

µm particle diameter) (LPW Technology Ltd., UK) via a RenAM 500 M (Renishaw, UK) SLM system. The RenAM 500 M utilizes a modulated laser system whereby the laser operates point-wise for a fixed exposure time and point distance. Thus, scanning speed is defined as point distance/exposure time. Point distance was set at a constant 45 µm with scan speed varied using exposure time. All samples were produced under argon atmosphere using a pre-heated substrate at 170℃ and 30 µm layer thickness.

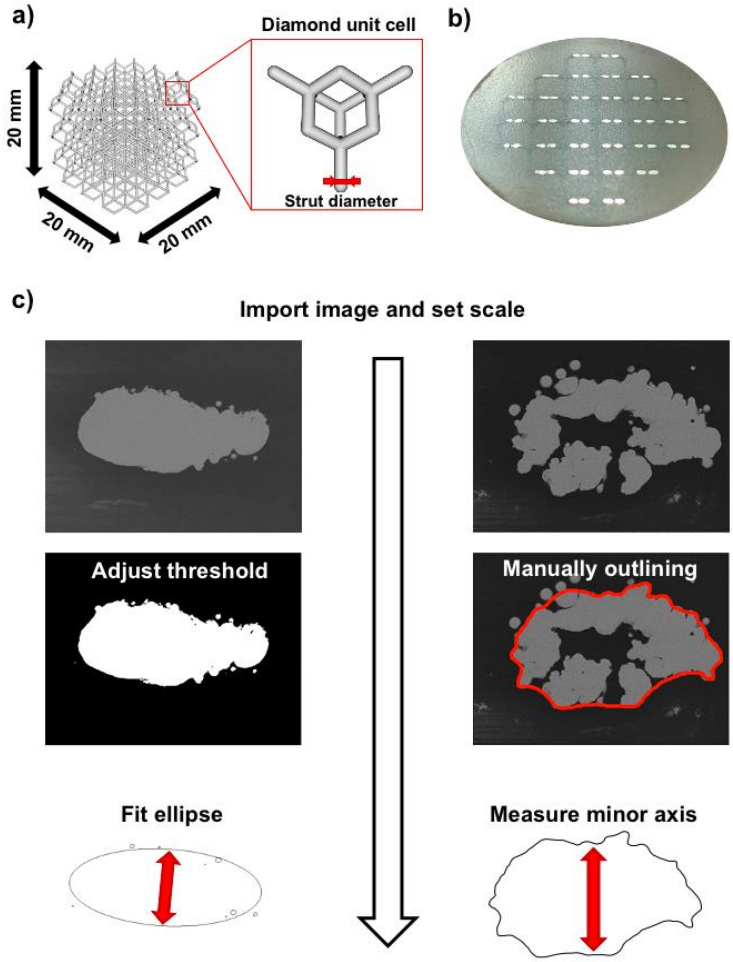


**Figure 2.** Images showing (a) the cuboidal and diamond unit cell design selected, (b) an example of cold-mounted and polished lattice and (c) a flow chart illustrating the contouring strategies used to measure strut diameter.

*2.2 Design of Experiment*

Two studies were performed. Within the first (Table I), SC specimens were produced with varying laser powers (50-150 W), scanning speeds (750-2250 mm/s) and strut diameters (150 μm, 250 μm and 350 μm). SC+F specimens were manufactured for the midpoint conditions, using 100 W and 1125 mm/s.

**Table I** DoE for the comparison of SC and SC+F scan strategy.

| Laser power (W) | Scan speed (mm/s) | Exposure time (µs) | Energy density (J/mm) | Scan strategy |
|---|---|---|---|---|
| 100 | 1125 | 40 | 0.089 | SC+F |
| 50 | 2250 | 20 | 0.022 | SC |
| | 1125 | 40 | 0.044 | |
| | 750 | 60 | 0.067 | |
| 100 | 2250 | 20 | 0.044 | SC |
| | 1125 | 40 | 0.089 | |
| | 750 | 60 | 0.133 | |
| 150 | 2250 | 20 | 0.067 | SC |
| | 1125 | 40 | 0.133 | |
| | 750 | 60 | 0.200 | |

The result of the first parametric analysis were used to develop a second study to better characterise the occurrence of porosity and dimensional accuracy (Table II). These parameters were selected to improve the resolution of the process window near the boundary between porous/fully dense lattices and successful/failed lattices of 250 µm strut diameter structures .

**Table II** Combination of parameters selected to evaluate the parametric effects on internal porosity of 250 µm lattice manufactured by SC.

| Laser power (W) | Scan speed (mm/s) | Exposure time (µs) | Energy density (J/mm) |
|---|---|---|---|
| 50 | 1250 | 36 | 0.040 |
| | 1000 | 45 | 0.050 |
| | 750 | 60 | 0.067 |
| 70 | 1750 | 26 | 0.040 |
| | 1500 | 30 | 0.047 |
| | 1250 | 36 | 0.056 |
| | 1000 | 45 | 0.070 |
| 90 | 2250 | 20 | 0.040 |
| | 2100 | 21 | 0.043 |
| | 1750 | 26 | 0.051 |
| | 1500 | 30 | 0.060 |
| | 1250 | 36 | 0.072 |
| | 1000 | 45 | 0.090 |
| 100 | 2250 | 20 | 0.044 |
| | 1125 | 40 | 0.089 |
| 105 | 2250 | 20 | 0.047 |
| | 2100 | 21 | 0.050 |
| | 1750 | 26 | 0.060 |
| | 1500 | 30 | 0.070 |
| | 1250 | 36 | 0.084 |
| 115 | 2250 | 20 | 0.051 |
| | 2100 | 21 | 0.055 |
| | 1750 | 26 | 0.066 |
| 150 | 2250 | 20 | 0.067 |

*2.3 Specimen Preparation*

Fabricated specimens were cut from the build substrate by Wire EDM, cleaned in a water bath to remove excess powder, air dried, and cold-mounted in resin (VersoCit-2 Powder, Struers Aps, Denmark). Samples were ground progressively from 220 to 4000 grit (Struers Aps, Denmark) With a final polishing performed using an activated Op-s suspension (Struers Aps, Denmark). Micrographs of 20 strut cross sections (Figure 2b) for each sample were captured using a Scanning Electronic Microscope (SEM, Hitachi TM3000, Japan) in backscattered (BSE) mode.

*2.4 Image Analysis and Process Mapping*

Micrographs were analysed with ImageJ (NIH, USA., 1.53a) (Schneider *et al.*, 2012). As shown in Figure 2c, strut contour was initially defined by an appropriate global threshold or via manual outline for fragmented sections. For both methods, the boundary included any internal pore areas. Individual struts within the lattice built at an angle of 54° resulting in an elliptical cross-section, thus, strut diameter was determined as the minor axis of a fit ellipse. Internal porosity was calculated as the total hollow area within struts divided by the total cross section area for all 20 struts in each sample. Process contour maps were plotted using MATLAB R2018b 9.5.0.944444 (MathWorks Inc. USA).

## 3. Results and Discussion

*3.1 SC and SC+F comparison*

Figure 3a compares mean strut thickness between SC and SC+F strategies for identical processing parameters (100 W, 1125 mm/s). SC+F strut diameter are on average 7% greater than those of SC for all sizes. Both SC and SC+F show a fully dense core for 150 µm and 250 µm struts, however greater diameters reveal the inability of the SC strategy to produce fully dense struts (Figure 3b) . This comparison demonstrates the feasibility of using SC as a method for producing fully dense thin lattice struts below a certain diameter. Nevertheless, the obtained geometric accuracy is relatively low with errors of 3.5%, -12.6% and -7.4% for 150 µm, 250 µm and 350 µm, respectively.

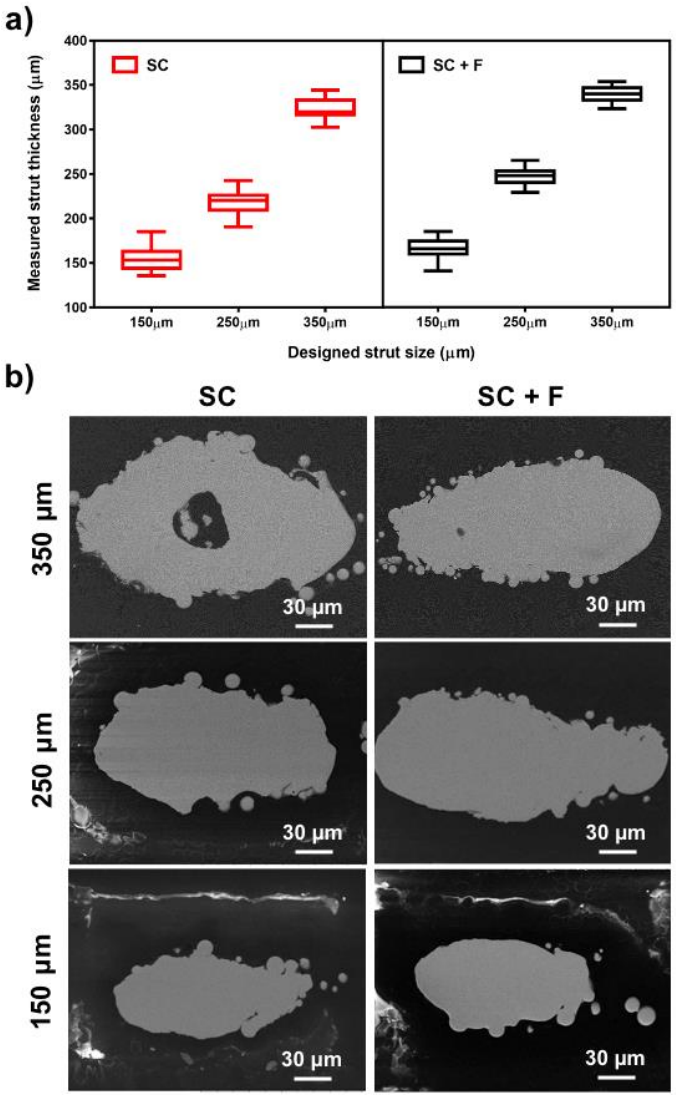

**Figure 3.** Comparison between SC and SC+F scan strategy under same processing parameters (laser power 100 W, scan speed 1125 mm/s): (a) strut thickness range for designed value of 150 μm, 250 μm and 350 μm; (b) SEM images showing different internal morphology under three designed strut thickness.

Previous studies have demonstrated that energy input influences melt pool width, directly relating it to strut thickness regardless of scan strategy used (Ghouse *et al.*, 2017, Onal *et al.*, 2019). SC+F produces greater energy input per strut than SC, even showing different energy input for adjacent struts; as illustrated in Figure 1b,1c, and 1d. The relatively limited conductive heat flow afforded by thin lattice struts results in a local thermal build-up during laser exposure whereby surplus energy simply drives up the melt pool width. In this scenario, final strut diameter is disproportionately driven by energy input as illustrated in the 150 μm struts where mean strut thicknesses are 155.2 μm and 165.7 μm for SC and SC+F respectively. Additionally, the previously highlighted differences in energy input between adjacent struts for the SC+F scan strategy are likely to induce further geometric inconsistencies. A similar phenomena was reported by Rashid et al. comparing single and double hatch scan (Rashida *et al.*, 2017) with thicker struts manufactured by double hatch scan due to the increase in energy input on each layer compared to single hatch scan. It should be noted however that the potential advantages of SC lattice production are limited by strut diameter. Above a threshold diameter, energy input and corresponding melt pool width become insufficient to produce a fully dense strut and internal porosity remains following processing as highlighted in the 350 μm SC sample in Figure 3b. Thus, it is clear that it is necessary to analyse the processing window of this scan strategy.

Processing maps indicating strut condition of lattices produced using SC are shown in Figure 4a-c. For the 150 μm strut diameter lattices, most parameters produced a fully dense material, nevertheless, manufacturing failed for 50 W, 1125 mm/s and 2250 mm/s due to insufficient energy input to form a stable structure (Figure 4a). Occurrence of internal porosity increased with strut diameter as revealed by the shift in solid core areas observed in 250 μm samples (Figure 4b) and 350 μm samples (Figure 4c). Corresponding pore fraction by cross-section area also increased with strut diameter from ~1.6% to ~27.3% for 250 μm and 350 μm lattice respectively (Figure 4b and 4c insets). Likewise the occurrence of porosity decreases with increasing energy density as demonstrated in the 350 μm specimens (Figure 4c) where the only fully dense struts occurred under greatest energy density (150 W and 750 mm/s – 1125 mm/s). This highlights that internal morphology of SC manufactured lattices is highly dependent on both strut thickness and processing parameters.

A strong linear relationship ($R^2 \geq 0.97$) between the energy density and resulting lattice strut diameter for each design strut thickness is shown in Figure 4d. This further confirms that, at these scales, process parameters as much as laser path govern the resulting geometry and careful control is essential for accurate lattice production. Single point exposure investigations have previously yielded positive results for lattice production showing the link between energy input and strut diameter (Mullen *et al.*, 2009, Onal *et al.*, 2019, Yan *et al.*, 2012). The SC strategy builds on this combining the control of both laser path and melt pool size via process parameter optimisation but eliminating the inconsistencies brought by hatch-filling.

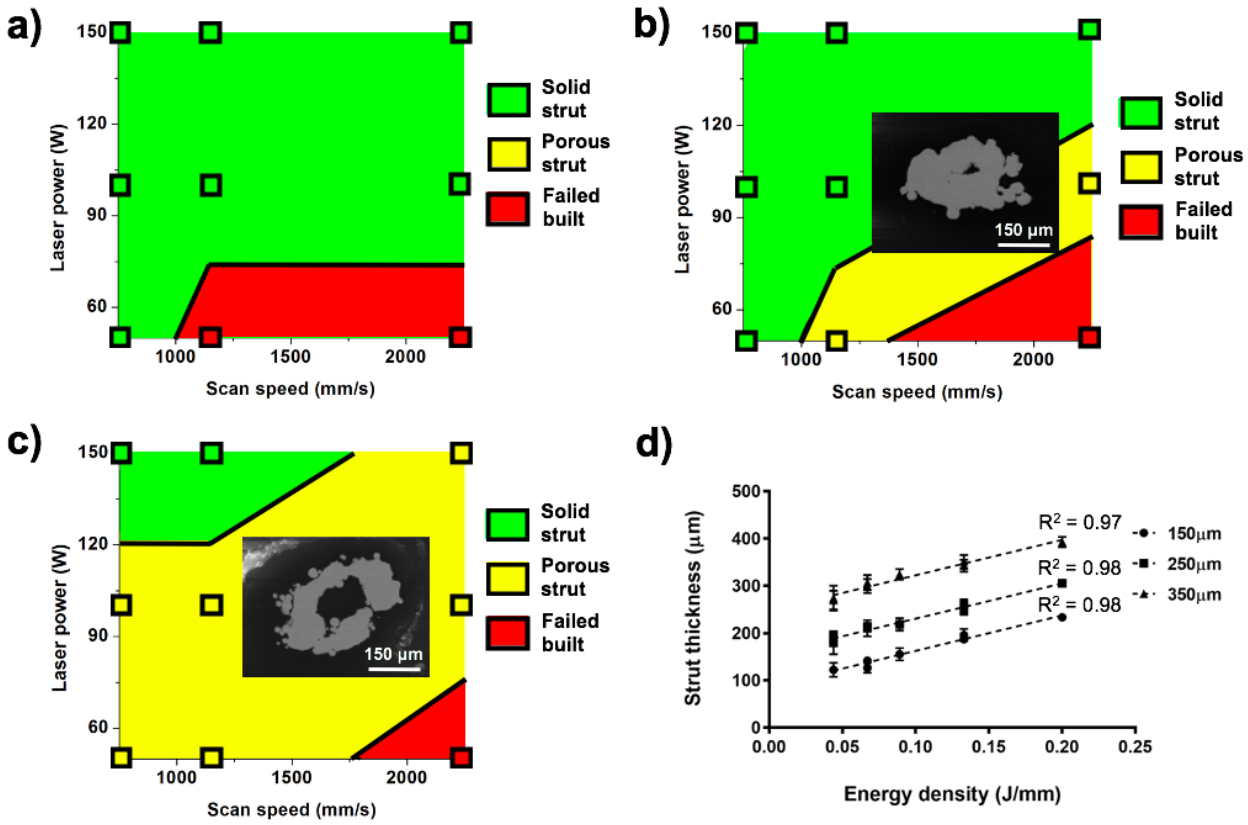


**Figure 4.** Parametric maps for strut thickness of (a) 150 µm, (b) 250 µm and (c) 350 µm, (a)-(c), where green areas represent struts built with solid core, yellow areas struts built with hollow structures and red areas unsuccessful built with SEM details showing the variation of hole area; and (d) correlation between energy density and strut thickness.

Other research has confirmed that increasing energy density raises melt pool width (Qiu *et al.*, 2015) which can be used to control the final strut diameter for a given SC laser path. To produce fully dense struts however, the melt pool width, and in turn the energy density, should be sufficient to melt the centre of each strut for a given laser path. A simplified geometric interpretation suggests that the smallest melt pool diameter needed to produce a fully dense strut is equal to the diameter of the laser path. This would produce a strut of diameter equal to approximately twice that of the melt pool. This relationship combined with process mapping may allow the input parameters themselves to act as the fine control for predictable geometric accuracy and strut integrity of SC processed lattices.

*3.2 Processing window of SC manufactured samples*

To improve and investigate the accuracy of this process mapping method, a further study was carried out using 250 µm strut diameter SC lattices. Process parameters near the solid/porous boundary were selected to accurately map this interface (Figure 5a). Internal porosity was revealed to be highly dependent on the energy density (Figure 5b), with hollow regions occupying 1.18% to 2.51% of the total area for values below 0.056 J/mm. As energy density increased from 0.056 J/mm to 0.089 J/mm, the corresponding porosity decreased, with fully dense struts obtained where energy density was greater than 0.089 J/mm. Significant porosity was observed under low laser powers and high scan speeds (Figure 5c). This results from the limited energy transferred, either due to low input energy overall or the brief laser/bed interaction time, reducing melt pool diameter. Nevertheless, there was no direct correlation between porosity and either laser power or scanning speed, suggesting a combination of both parameters as the main driver of the observed trends (Figure 5c).

This expanded study reveals that the relationship between energy density and accuracy follows a convex unimodal trend with the minimum located at ~0.1 J/mm, resulting in standard error below 0.1% and fully dense struts (figure 5d). Furthermore, discrepancy between design and actual strut

diameter is minimised at 0.1 J/mm (150 W, 1500 mm/s). It is worth mentioning the fully dense struts were produced up to the maximum energy density, 0.2 J/mm (Figure 4b), indicating that careful selection and control of energy density, via scan speed and laser power, can be used to effectively manufacture lattices with SC strategy.

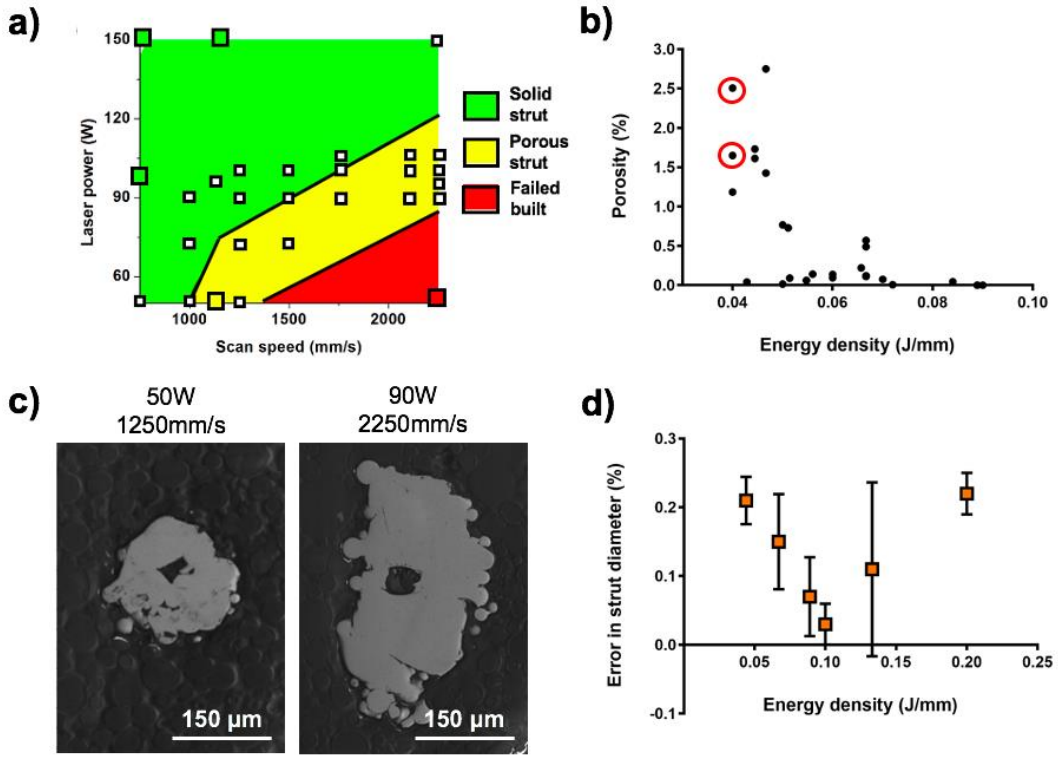


**Figure 5.** Images showing (a) parameters selection (white cubic dots), (b) influence of energy density on internal porosity; (c) SEM micrographs presenting the internal porosity of the two red circled parameters in (a) and (b), respectively and (d) plot demonstrating the strut size error (%) as a result of energy density variations.

Data from both studies can be combined to form a 250 µm process map of both strut diameter and porosity (Figure 6). The relationship between strut diameter and laser power (W) and scan speed (mm/s) can be fitted to a plane (Figure 6a) with a standard error of estimate, $\sigma_{est}$, of 13.8 µm ($R^2 = 0.77$) which is reasonable given the method of measurement and irregularity of strut cross section in some cases. The plane has the equation:

$$\text{Strut Diameter } (\mu m) = 0.8423 * \text{Power (W)} - 0.0326 \text{ Speed (mm/s)} + 190.4728 \qquad \textit{-Equation 2}$$

Isolines derived from this planar fit are shown super-imposed over the contour plot of porosity in Figure 6b to form a process map. Fully dense (yellow) regions can easily be seen alongside the

corresponding expected strut diameter for the 250 μm design condition. Maps of this form could be produced to parametrically adjust strut geometry when using the SC strategy.

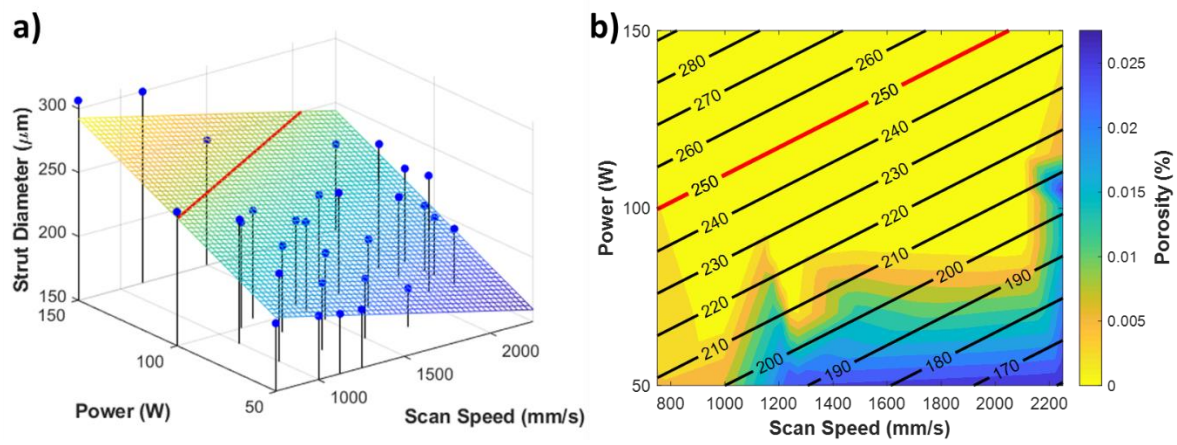


**Figure 6.** Process map for the combined data of both studies. (a) 3D scatter plot showing strut diameter vs laser power (W) and scan speed (mm/s) with target 250 μm condition shown by red line. (b) Process map displaying both strut diameter (labelled contour lines) and porosity (colour map) with laser power (W) and scan speed (mm/s) with target 250 μm strut diameter highlighted in red.

*3.3 Wider Biomedical Implications*

This study has highlighted how process parameters and laser scan strategy combine with the design to form the manufactured geometry for fine lattice structures. Understanding and control of these inputs will be critical in the translation of devices incorporating lattices from research to clinical use. Previous studies have shown how lattice density (Tobias Maconachie, 2019, Soro *et al.*, 2019) and strut diameter (Chunlei Qiu, 2015) influence mechanical properties; how pore size influences cell proliferation (Markhoff *et al.*, 2015, Li *et al.*, 2020); and how relative density can govern MRI artefacts (Luke N. Carter, 2020), or novel drug delivery (Burton *et al.*, 2019). All of these novel functionalities rely on accurate, reproducible, and robust methods of lattice manufacture to ensure the closest possible alignment of design and manufactured geometry.

By constructing process maps similar to those presented, it is possible to gain confidence that lattices will be produced 'first-time-right' when integrated in to larger implants. Likewise the SC scanning strategy aims to reduce uncontrolled variability introduced at the slicing stage. Both of these aspects will be critical, from both a patient welfare and regulatory perspective, to ensure that devices perform as intended when implanted.

## 4. Conclusions

In this work, the capability of SC to manufacture lattice structures with thin struts of diameter less than 350 μm has been demonstrated. Two studies have highlighted relationships between strut density and geometric accuracy showing the potential for fine control of lattice manufacture via parametric adjustment alongside the limit of such approach. Linear energy density is suggested as a practical indicator of the process, from which both the accuracy and internal morphology of lattice struts could be predicted and optimised. The process maps generated may be used in future lattice production as a practical method for structural control. It is hoped that the use of SC processes lattice will improve geometric consistency critical for the full exploitation of AM lattices in medical devices.

**Funding:** This work was supported by the EPSRC funded project: Process Design to Prevent Prosthetic Infections (EP/P02341X/1).

The authors declare no conflict of interest.

## References


BURTON, H. E., EISENSTEIN, N. M., LAWLESS, B. M., JAMSHIDI, P., SEGARRA, M. A., ADDISON, O., SHEPHERD, D. E. T., ATTALLAH, M. M., GROVER, L. M. & COX, S. C. 2019. The design of additively manufactured lattices to increase the functionality of medical implants. *Mater. Sci. Eng., C,* 94**,** 901-908.

CARTER, L. N., ADDISON, O., NAJI, N., SERES, P., WILMAN, A. H., SHEPHERD, D. E. T., GROVER, L. M. & COX, S. C. 2020. Reducing MRI susceptibility artefacts in implants using additively manufactured porous Ti-6Al-4V structures. *Acta Biomater.,* 107**,** 338-348.

CHUNLEI QIU, S. Y., NICHOLAS J.E. ADKINS, MARK WARD, HANY HASSANIN, PETER D. LEE, PHILIP J. WITHERS, MOATAZ M. ATTALLAH 2015. Influence of processing conditions on strut structure and compressive properties of cellular lattice structures fabricated by selective laser melting. *Materials Science & Engineering A,* 628**,** 188-197.

DEING, A., LUTHRINGER, B. L., LAIPPLE, D., EBEL, T. & WILLUMEIT, R. 2014. A Porous TiAl6V4 Implant Material for Medical Application. *Int. J. Biomater.,* 2014**,** 8.

GHOUSE, S., BABU, S., VAN ARKEL, R. J., NAI, K., HOOPER, P. A. & JEFFERS, J. R. T. 2017. The influence of laser parameters and scanning strategies on the mechanical properties of a stochastic porous material. *Mater. Des.,* 131**,** 498-508.

GROßMANN, A., FELGER, J., FRÖLICH, T., GOSMANN, J. & MITTELSTEDT, C. 2019. Melt pool controlled laser powder bed fusion for customised low-density lattice structures. *Mater. Des.,* 181**,** 108054.

GU, H., GONG, H., PAL, D., RAFI, K., STARR, T. & STUCKER, B. 2013. Influences of Energy Density on Porosity and Microstructure of Selective Laser Melted 17- 4PH Stainless Steel. *Solid Freeform Fabr. Symp.,* 474**,** 474-489.

HEDAYATI, R., SADIGHI, M., MOHAMMADI-AGHDAM, M. & HOSSEINI-TOUDESHKY, H. 2018. Comparison of elastic properties of open-cell metallic biomaterials with different unit cell types. *J. Biomed. Mater. Res. B Appl. Biomater.,* 106**,** 386-398.

HONG, M. H., MIN, B. K. & KWON, T.-Y. 2016. The Influence of Process Parameters on the Surface Roughness of a 3D-Printed Co–Cr Dental Alloy Produced via Selective Laser Melting. *Appl. Sci.,* 6**,** 401.

KHORASANIA, A., GIBSOND, I., AWANA, U. S. & GHADERI, A. 2019. The effect of SLM process parameters on density, hardness, tensile strength and surface quality of Ti-6Al-4V. *Addit. Manuf.,* 25**,** 176-186.

KOPTYUG, A., RÄNNAR, L. E., BÄCKSTROM, M., FAGER FRANZÉN, S. F. & DÉRAND, P. 2013. Additive Manufacturing Technology Applications Targeting Practical Surgery. *Int. J. Life Sci. Med. Res.,* 3**,** 15-24.

KUSUMA, C., AHMED, S. H., MIAN, A. & SRINIVASAN, R. 2017. Effect of Laser Power and Scan Speed on Melt Pool Characteristics of Commercially Pure Titanium (CP-Ti). *J. Mater. Eng. Perform.,* 26**,** 3560-3568.

LI, B., HESAR, B. D., ZHAO, Y. & DING, L. 2020. Design and additive manufacturing of porous titanium scaffolds for optimum cell viability in bone tissue engineering. *Proceedings of the Institution of Mechanical Engineers. Part B, Journal of engineering manufacture***,** 95440542093756.

LUKE N. CARTER, O. A., NASHWAN NAJI, PETER SERES, ALAN H. WILMAN, DUNCAN E.T. SHEPHERD, LIAM GROVER, SOPHIE COX 2020. Reducing MRI susceptibility artefacts in implants using additively manufactured porous Ti-6Al-4V structures. *Acta Biomaterialia,* 107**,** 338-348.

MAAMOUN, A. H., XUE, Y. F., ELBESTAWI, M. A. & VELDHUIS, S. C. 2018. Effect of Selective Laser Melting Process Parameters on the Quality of Al Alloy Parts: Powder Characterization, Density, Surface Roughness,and Dimensional Accuracy. *Materials,* 11**,** 2343.

MAIETTA, S., GLORIA, A., IMPROTA, G., RICHETTA, M., DE SANTIS, R. & MARTORELLI, M. 2019. A Further Analysis on Ti6Al4V Lattice Structures Manufactured by Selective Laser Melting. *J. Healthc. Eng.,* 2019**,** 9.

MARKHOFF, J., WIEDING, J., WEISSMANN, V., PASOLD, J., JONITZ-HEINCKE, A. & BADER, R. 2015. Influence of Different Three-Dimensional Open Porous Titanium Scaffold Designs on Human Osteoblasts Behavior in Static and Dynamic Cell Investigations. *Materials,* 8**,** 5490-5507.

MULLEN, L., STAMP, R. C., BROOKS, W. K., JONES, E. & SUTCLIFFE, C. J. 2009. Selective Laser Melting: A Regular Unit Cell Approach for the Manufacture of Porous, Titanium, Bone In-Growth Constructs, Suitable for Orthopedic Applications. *Wiley,* 89B**,** 325-334.

MURR, L. E. 2020. Metallurgy principles applied to powder bed fusion 3D printing/additive manufacturing of personalized and optimized metal and alloy biomedical implants: an overview. *J. Mater. Res. Technol.,* 9**,** 1087–1103.

NGUYEN, D. S., PARK, H. S. & LEE, C. M. 2020. Optimization of selective laser melting process parameters for Ti-6Al-4V alloy manufacturing using deep learning. *J. Manuf. Process,* 55**,** 230-235.

NICKELS, L. 2020. Software toolkits for architected materials, lightweighting, and more. *Met. Powder Rep.*

ONAL, E., MEDVEDEV, A. E., LEEFLANG, M. A., MOLOTNIKOV, A. & ZADPOOR, A. A. 2019. Novel microstructural features of selective laser melted lattice struts fabricated with single point exposure scanning. *Addit. Manuf.,* 29**,** 100785.

QIN, Q. & CHEN, G. X. 2013. Effects of Parameters on Surface Roughness of Metal Parts by Selective Laser Melting. *Adv. Mater. Res.,* 834**,** 872-875.

QIU, C., YUE, S., ADKINS, N. J. E., WARD, M., HASSANIN, H., LEE, P. D., WITHERS, P. J. & ATTALLAH, M. M. 2015. Influence of processing conditions on strut structure and compressive properties of cellular lattice structures fabricated by selective laser melting. *Mater. Sci. Eng., A,* 628**,** 188-197.

RASHIDA, R., MASOODA, S. H., RUANA, D., PALANISAMY, S., RASHID, R. A. R. & BRANDT, M. 2017. Effect of scan strategy on density and metallurgical properties of 17-4PH parts printed by Selective Laser Melting (SLM). *J. Mater. Process. Technol.,* 249**,** 502-511.

SALEM, H., CARTER, L. N., ATTALLAH, M. M. & SALEM, H. G. 2019. Influence of processing parameters on internal porosity and types of defects formed in Ti6Al4V lattice structure fabricated by selective laser melting. *Mater. Sci. Eng., A,* 767**,** 138387.

SCHNEIDER, C. A., RASBAND, W. S. & ELICEIRI, K. W. 2012. NIH Image to ImageJ: 25 years of image analysis. *Nat. Methods,* 9**,** 671-675.

SHIPLEY, H., MCDONNELL, D., CULLETON, M., COULL, R., LUPOI, R., O'DONNELL, G. & TRIMBLE, D. 2018. Optimisation of process parameters to address fundamental challenges during selective laser melting of Ti-6Al-4V: A review. *Int. J. Mach. Tools Manuf.,* 128**,** 1-20.

SONG, B., DONG, S., ZHANG, B., LIAO, H. & CODDET, C. 2012. Effects of processing parameters on microstructure and mechanical property of selective laser melted Ti6Al4V. *Mater. Des.,* 35**,** 120-125.

SORO, N., ATTAR, H., WU, X. & DARGUSCH, M. S. 2019. Investigation of the structure and mechanical properties of additively manufactured Ti-6Al-4V biomedical scaffolds designed with a Schwartz primitive unit-cell. *Materials Science and Engineering: A,* 745**,** 195-202.

TOBIAS MACONACHIE, M. L., BILL LOZANOVSKI, XUEZHE ZHANG, MA QIAN, OMAR FARUQUE, MILAN BRANDT 2019. SLM lattice structures: Properties, performance, applications and challenges. *Materials and Design,* 183.

TREVISAN, F., CALIGNANO, F., LORUSSO, M., PAKKANEN, J., AVERSA, A., AMBROSIO, E. P., LOMBARDI, M., FINO, P. & MANFREDI, D. 2017. On the Selective Laser Melting (SLM) of the AlSi10Mg Alloy: Process, Microstructure, and Mechanical Properties. *Materials,* 10**,** 76.

VAN BAEL, S., CHAI, Y. C., TRUSCELLO, S., MOESEN, M., KERCKHOFS, G., VAN OOSTERWYCK, H., KRUTH, J. P. & SCHROOTEN, J. 2012. The effect of pore geometry on the in vitro biological behavior of human periosteum-derived cells seeded on selective laser-melted Ti6Al4V bone scaffolds. *Acta Biomaterialia,* 8**,** 2824-2834.

VILLAPÚN, V. M., CARTER, L. N., GAO, N., ADDISON, O., WEBBER, M. A., SHEPHERD, D. E. T., ANDREWS, J. W., LOWTHER, M., AVERY, S., GLANVILL, S. J., GROVER, L. M. & COX, S. C. 2020. A design approach to facilitate selective attachment of bacteria and T mammalian cells to additively manufactured implants. *Addit. Manuf.,* 36**,** 101528.

WANG, L. Z., WANG, S. & WU, J.-J. 2017. Experimental investigation on densification behavior and surface roughness of AlSi10Mg powders produced by selective laser melting. *Opt. Laser Technol.,* 96**,** 88-96.

YAN, C., HAO, L., HUSSEIN, A. & RAYMONT, D. 2012. Evaluations of cellular lattice structures manufactured using selective laser melting. *Int. J. Mach. Tools Manuf.,* 62**,** 32-38.

YAN, C., HAO, L., HUSSEIN, A., YOUNG, P. & RAYMONT, D. 2014. Advanced lightweight 316L stainless steel cellular lattice structures fabricated via selective laser melting. *Mater. Des.,* 55**,** 533-541.

YUSUF, S. M. & GAO, N. 2017. Influence of energy density on metallurgy and properties in metal additive manufacturing. *Mater. Sci. Technol.,* 33**,** 1269-1289.